npj | Quantum Materials

www.nature.com/npjquantmats

ARTICLE OPEN

Investigation on the phase-transition-induced hysteresis in the thermal transport along the *c*-axis of $MoTe_2$

Xue-Jun Yan[1], Yang-Yang Lv[1], Lei Li[1], Xiao Li[2], Shu-Hua Yao[1,3], Yan-Bin Chen[2,3], Xiao-Ping Liu[1,3], Hong Lu[1,3], Ming-Hui Lu[1,3] and Yan-Feng Chen[1,3]

The storage and recall of thermal information can be achieved by a thermal memory, which is a key element in the applications of thermal logic devices. Thermal memories can be experimentally realized by solid-state materials with hysteretic thermal transport properties. Here, by means of the time-domain thermoreflectance method, we observe hysteretic behaviors in the *c*-axis thermal conductivities of molybdenum ditelluride ($MoTe_2$) in their metastable phases. Supported by the characterizations of Raman modes and electrical resistivity, we infer that this hysteresis is induced by the structural phase transition around 250 K. This thermal hysteresis is dominated by the transportation of phonons and makes it possible to build all-phononic devices based on $MoTe_2$. In addition, the mechanism of phonon scatterings is analyzed quantitatively using Boltzmann transport equation. This study provides a promising material system for applications in integrated phononic devices, topological electronics and thermoelectric materials.

npj Quantum Materials (2017)2:31 ; doi:10.1038/s41535-017-0031-x

INTRODUCTION

The microelectronic devices capable of high-speed computing have a broad range of applications nowadays. Among them, electronic memory is one of the key logic devices that store and retrieve information by manipulating electrical charges or magnetism.[1, 2] However, its counterpart 'thermal memory' remains unavailable for the storage of thermal or phononic information in practice. A theoretical model of thermal memory has already been proposed in a nonlinear lattice,[3] but the majority of experimental realizations in this field are based on the phase change materials (PCMs) with hysteretic thermal properties.[4–6] In some traditional PCMs, e.g., vanadium dioxide (VO_2), the hystereses of thermal conductivities are mainly resulted from the hysteretic transportations of electrons during the phase transitions.[7, 8] Due to the weak electron-phonon couplings, these PCMs may be incompatible with the 'all-phononic devices'.[9] In addition, their hysteretic performances are highly sensitive, for example, to the stoichiometry, sizes and even microstructures of the PCM thin films,[10–12] and these factors are difficult to be controlled precisely in the synthesis processes. Therefore, it is necessary to explore more materials with simple chemical components to realize the hysteretic behavior of thermal transport that is dominantly contributed by phonons.

Molybdenum ditelluride ($MoTe_2$) is a typical layered material with abundant structural phases,[13] i.e., 2 H ($P6_3/mmc$), 1 T′ ($P2_1/m$) and Td ($Pmn2_1$) phases. The structural phase transition from the high-temperature 1T′-phase to the low-temperature Td-phase around 250 K had been studied decades ago. In these literatures, researchers emphasized on the abnormal thermal hysteresis of the electrical resistivity,[14, 15] which was believed to be induced by the hysteretic effect of the crystalline structure according to the characterizations of high-resolution X-ray diffraction (XRD),[16] electron diffraction,[17] and Raman spectroscopy.[18, 19] The thermal conductivity of this material system is expected to show a similar thermal hysteresis because it can be remarkably affected by lattice vibrations or the collective excitation, phonons. However, to the best of our knowledge, the evolution of thermal properties during the structural phase transition has never been studied in the metastable phase of $MoTe_2$, which may be a promising candidate for the practical applications of thermal memory. Furthermore, $MoTe_2$ is a typical transition metal dichalcogenides (TMDs) materials which have been intensively studied recently due to their promising applications in the next-generation electronics, opto-electronics, and valleytronics.[20] It has been demonstrated that the quantum spin Hall effect[21] and the Weyl fermions[22–25] can be realized in TMDs. Specifically, it has been predicted that the phase transition in $MoTe_2$ may lead to a change of the band topology, which can be regarded as the topological phase transition.[26, 27] It is known that heat dissipation can be a big issue in microelectronic device performances. In order to apply $MoTe_2$ into a practical application, it is important to investigate its intrinsic thermal properties, especially to understand its thermal transport behavior.

In this work, we measured the thermal conductivities of $MoTe_2$ samples along the *c*-axis by the time-domain thermoreflectance (TDTR) method from 80 to 300 K. The temperature dependence of measured thermal conductivity was investigated by a Boltzmann transport equation (BTE) considering the anisotropic properties of the layered structures. The mechanisms of phonon scatterings, as well as several intrinsic parameters of the 2H-phase and metastable phase $MoTe_2$ samples were analyzed quantitatively using this model. The hysteretic behavior of thermal conductivity around 250 K was observed for the first time in the metastable $MoTe_2$ samples quenched from high temperatures. The maximum difference of the hysteresis loop is ~10%, which is comparable to that of the state-of-the-art PCMs. We found that this phenomenon

[1]National Laboratory of Solid State Microstructures & Department of Materials Science and Engineering, College of Engineering and Applied Sciences, Nanjing University, 210093 Nanjing, China; [2]National Laboratory of Solid State Microstructures & Department of Physics, Nanjing University, 210093 Nanjing, China and [3]Collaborative Innovation Center of Advanced Microstructures, Nanjing University, 210093 Nanjing, China
Correspondence: Hong Lu (hlu@nju.edu.cn) or Ming-Hui Lu (luminghui@nju.edu.cn)

Received: 2 January 2017 Revised: 15 April 2017 Accepted: 9 May 2017
Published online: 19 June 2017

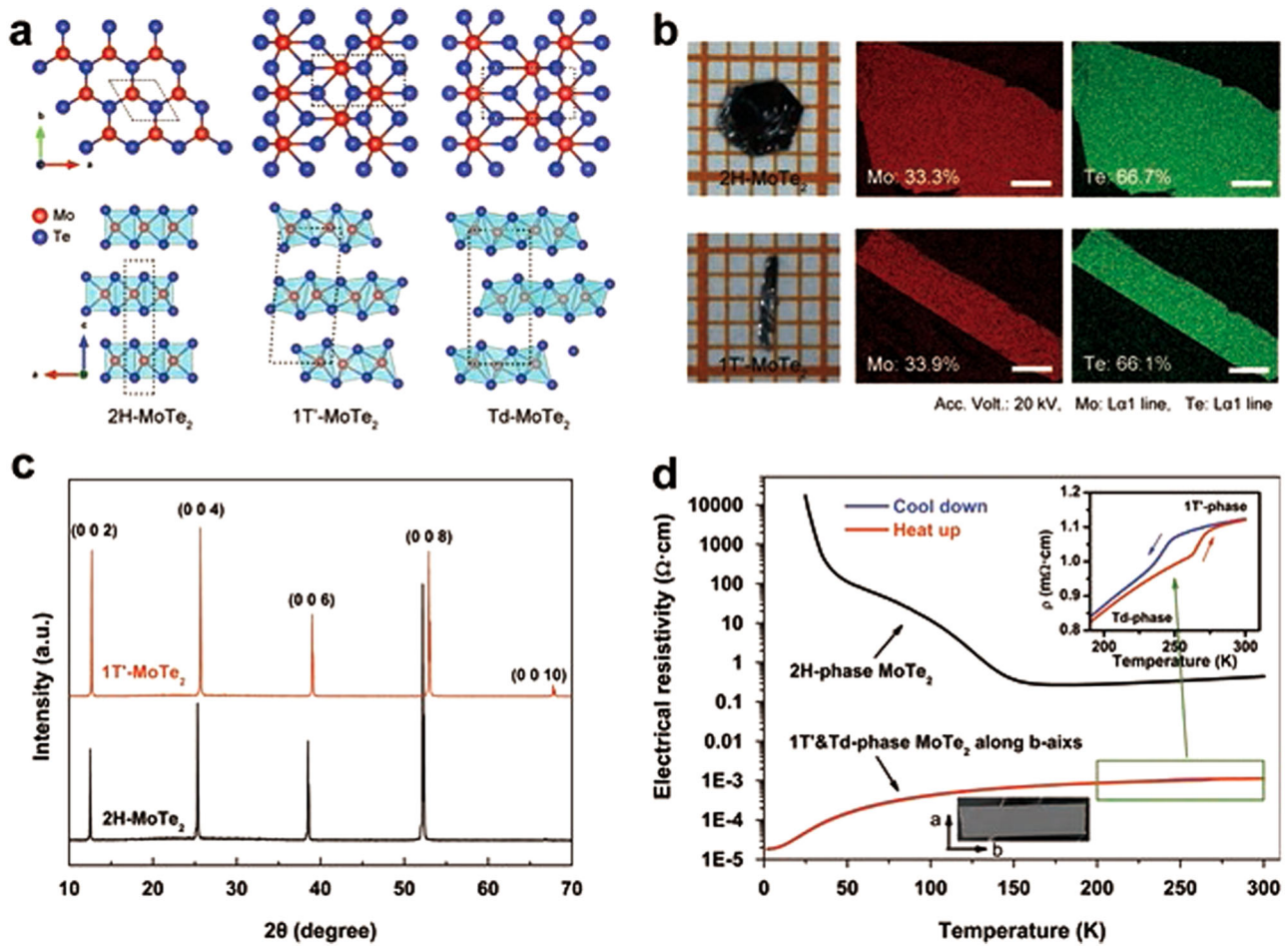

Fig. 1 **a** Crystal structures of 2H-phase (α-), 1T′-phase (β-) and Td-phase $MoTe_2$ along *c*-axis and *b*-axis. **b** Photographs of the as-grown $MoTe_2$ flakes in the 2H-phase and 1T′-phases and the corresponding EDS mapping. **c** XRD patterns of 2H-phase and 1T′-phase $MoTe_2$ samples. **d** Temperature dependence of electrical resistivity in the 2H-phase and 1T′-phase $MoTe_2$ samples along *b*-axis. The enlarged inset is the thermal hysteresis of electrical resistivity in the 1T′-phase $MoTe_2$ at 200~300 K

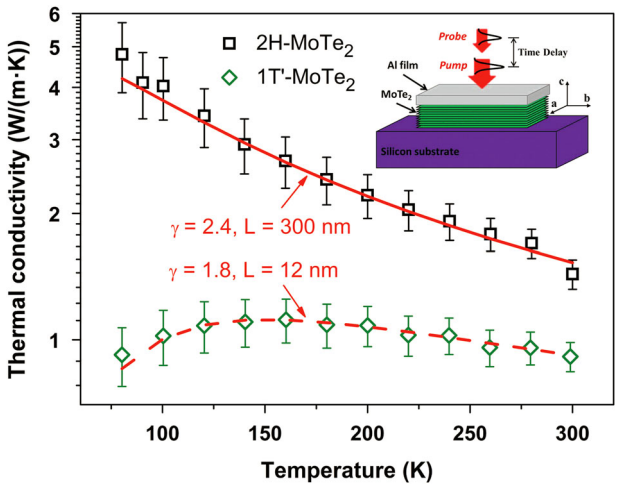

Fig. 2 Thermal conductivity of 2H-$MoTe_2$ and 1 T′-$MoTe_2$ samples in *c*-axis measured at 80–300 K. *Error bars* represent the systematic errors that are propagated from the uncertainties in film thickness, laser spot size, and specific heat of each layer, etc. The calculated results by our theoretical model are plotted as the *solid* and *dashed red lines* for the two samples, respectively. Inset: the schematic of TDTR measurements for the bulk $MoTe_2$ sample in this work

was closely related to the structural phase transition from the high-temperature 1T′-phase to the low-temperature Td-phase according to the consistent thermal hystereses of Raman spectra and electrical resistivity. Therefore, the thermal hysteresis of thermal conductivity here is dominated by the phonon transportations. This phonon manipulation in metastable $MoTe_2$ makes it possible to employ this material system for the applications of 'all-phononic' thermal memories.

RESULTS

In general, the crystal structures of $MoTe_2$ can be described as 'Te–Mo–Te' sandwiched layers separated by Van der Waals gaps (see Fig. 1a). The trigonal prismatic 2H-phase (or called α-phase) is the stable structure commonly existing at room temperature. The monoclinic 1T′-phase (or called β-phase) is the metastable structure formed at high temperatures (>900 °C) and it can be retained to room temperature by quenching treatments. The orthorhombic Td-phase can be transformed from 1T′-phase after being cooled down to low temperatures (<250 K). We synthesized $MoTe_2$ samples by the chemical vapor transport (CVT) method. To get the metastable 1T′-phase $MoTe_2$, we raised the growth temperature to 900–1000 °C and quenched the samples immediately to retain this high-temperature phase. The yielded 2H-$MoTe_2$ single crystals are hexagonal flakes with an average size of ~5 ×

5×0.05 mm while the 1T′-$MoTe_2$ are striped flakes due to the quasi-1D 'Mo–Mo' zigzag chains along *b*-axis. From the energy-dispersive spectroscopy (EDS) results in Fig. 1b, the distributions of chemical elements are uniform and the stoichiometric ratios (Mo: Te) are close to the ideal 1:1 in both cases. The slight deficiency of Te element in 1T′-$MoTe_2$ may result from the volatilization of high-vapor-pressure Te element at a higher growth temperature. The XRD patterns of the 2H-$MoTe_2$ and 1T′-$MoTe_2$ samples at room temperature are depicted in Fig. 1c. The sharp peaks with a full width at half maximum of ~0.07° indicate the high crystalline qualities of samples and the (0 0 *l*) peaks suggests that the exposed surfaces of samples were perpendicular to the *c*-axis. The lattice constants in *c*-axis were 14.050 and 13.895 Å according to the XRD peaks for 2H-$MoTe_2$ and 1T′-$MoTe_2$, respectively, in good agreement with the results reported previously.[28, 29] We measured the electrical resistivity along *b*-axis by a standard four-probe method at low temperatures and the results are shown in Fig. 1d. 2H and 1T′-$MoTe_2$ reveals the semiconducting and metallic characters that has been demonstrated before.[14, 30] It should be noted that an abnormal thermal hysteresis of electrical resistivity around 250 K is shown in the inset, indicating the phase transition from high-temperature 1T′-phase to Td-phase occurred in our metastable phase samples.[14, 15]

We measured the thermal conductivities along *c*-axis (κ_c) of the layered $MoTe_2$ samples by the TDTR method in a configuration shown in the inset of Fig. 2. We found that TDTR was quite suitable for the κ_c measurements of thin flakes with small and irregular dimensions comparing to other commercial instruments. Measured κ_c of 2H-phase and 1T′-phase (β-phase) $MoTe_2$ samples at the temperature range of 80–300 K are displayed in Fig. 2. For $MoTe_2$ in the 2H-phase, the κ_c increases linearly with the decrement of temperature and no saturation occurs until 80 K. The κ_c of the 1T′-phase $MoTe_2$ sample is lower in the same temperature range and it reaches a maximum value at ~160 K. We estimated the thermal conductivities in *a*-axis and *b*-axis were 50 times higher than that along *c*-axis empirically. This assumption would only introduce an error within 3% to the final results because the lateral thermal transport was negligible in these measurements with a high modulation frequency of 9.8 MHz.

According to our measurements, the *c*-axis thermal conductivity of $MoTe_2$ is mainly contributed by phonons, where the electron contribution is negligible (see supplemental information). To investigate the mechanism of phonon scatterings in our samples, we utilized an analytic solution based on the BTE[31] to fit our experimental results. In this model, the thermal conductivity along *c*-axis of the highly anisotropic material can be rewritten

$$\kappa_c = 2\pi A \int_{-1}^{1}\int_{0}^{1} C_{\mathbf{k}} v_{c,k} \tau_{\mathbf{k}} \hat{k}^2 d\hat{k} d\mu$$
$$= 2\pi A \int_{-1}^{1}\int_{0}^{1} N k_B [x/\sinh x]^2 v_{c,k} \tau_{\mathbf{k}} \hat{k}^2 d\hat{k} d\mu,$$

where $x = \hbar\omega_{(\mathbf{k})}/2k_BT$, $C_{\mathbf{k}}$ represents the specific heat of each phonon mode, $v_{c,k}$ is the acoustic velocity long *c*-axis, $\tau_{\mathbf{k}}$ is the relaxation time of phonons, $\mathbf{k}$ is the phonon wave vector, $\hat{k}$ is the normalized wave vector, $\omega_{(\mathbf{k})}$ is the phonon frequency, k_B is the Boltzmann constant, T is the temperature and A is a constant related to the volume of the Brillouin zone in reciprocal space. Considering the anisotropic properties of layered materials here, we used an anisotropic Debye model[32, 33] in which the phonon dispersion can be expressed as $\omega_{(\mathbf{k})}{}^2 = v_{ab}^2 k_{ab}^2 + v_c^2 k_c^2$, where *v* and *k* are the velocity and wave vector of phonons, respectively, and the footnotes indicate the corresponding parameters along *ab*-axis and *c*-axis. Even though the linear dispersion in Debye model is not very accurate to describe the transport property of phonons, it is sufficient for us to get the predominant mechanism of phonon scatterings in this work. Two types of phonon scatterings are considered here. The first one is the Umklapp scattering or the phonon-phonon scattering with a relaxation time of $\tau_U^{-1} = \frac{\hbar\gamma^2\omega_{(\mathbf{k})}^2}{Mv_c^2\Theta_D} \cdot T \cdot \exp(-\Theta_D/3T)$, where γ is the Grüneisen constant, M is the molar mass, Θ_D is the Debye temperature.[34] The other one is the boundary scattering whose relaxation time is $\tau_B^{-1} = \frac{v_c}{L}$, where L reflects the average distance of boundaries or grains. We estimated $\Theta_D = 135$ K, $v_c = 2000$ m/s and $v_{ab} = 8000$ m/s in $MoTe_2$ from literatures[35, 36] and calculated the total relaxation time $\tau^{-1} = \tau_U^{-1} + \tau_B^{-1}$ according to the Matthiessen's rule. Two key parameters reflecting the structural properties of samples, i.e., γ and L, were utilized to fit the temperature-dependent thermal conductivities. The fitting curves are shown as the *solid* and *dashed red lines* in Fig. 2. The effective Grüneisen constants γ are 2.4 and 1.8 for 2H-phase and 1T′-phase $MoTe_2$, respectively. The relative larger value for 2H-$MoTe_2$, which indicates a higher phonon nonlinearity, may be related to its larger lattice constant and weaker binding strength than that of 1T′-$MoTe_2$. These effective Grüneisen constants are close to the mean theoretical values for some typical TMDs,[37] e.g., 1.72 for $MoSe_2$ and 2.17 for WS_2, verifying the applicability of this model to describe the phonon-phonon scattering process in $MoTe_2$. The average distance L is 300 nm for 2H-$MoTe_2$, while it is only 12 nm for 1T′-$MoTe_2$. It indicates the strong boundary scatterings in the metastable phase sample, which may result from the high-density boundaries within the two co-existent phases, i.e., 1T′-phase and Td-phase, as well as the stacking disorders introduced during the fast quenching. Recently, it was discovered that the electrochemical intercalation could induce a structural phase transition from semiconducting 2H to metallic 1T phase in bulk molybdenum disulfide (MoS_2) samples.[38] The authors claimed that the increased phonon-boundary scattering and decreased thermal conductivity were resulted from the co-existence of these two phases and the stacking disorder, which agrees with our assumptions here. In brief, the $MoTe_2$ sample in 2H-phase reveals a feature of high-quality single crystal while the metastable 1T′-$MoTe_2$ behaves more like a poly-crystal according to the temperature dependence of thermal conductivity. These TDTR measurements and calculations offer us a convenient way to characterize the micro-structures of layered materials quantitatively.

We further measured the κ_c of the metastable phase $MoTe_2$ at a temperature range of 200–300 K in detail to obtain the temperature evolution of thermal properties during the phase transition. Two methods were applied to characterize the thermal conductivities in both warming up and cooling down routes. The first method labeled as 'the static method' was to measure κ_c by routine TDTR at each temperature stabilized for 1 h. In this way, we can get the intrinsic thermal properties despite of the temperature sweeping rate and minimize the thermal lag effect during any phase transition. The resulting discrete data are shown as the scatters in Fig. 3, whose values are the averages of five individual measurements. The second method labeled as 'the dynamic method' has been applied in the study of VO_2 thin films.[7] We recorded the ratio of in-phase and out-of-phase voltage $-V_{in}/V_{out}$ at a fixed delay time τ of 300 ps when sweeping the sample temperature continuously at a slow rate of ~0.04 K/s. The ratio $-V_{in}/V_{out}$ at each quasi-continuous temperature was fit by the thermal model with temperature-dependent heat capacity in order to acquire a series of effective thermal conductivity in real-time. The results of sample 1 & 2 measured by this dynamic method match sufficiently well with those from the static method, showing the accuracy and reliability of each method. It should be noted that the dynamic method can monitor the transient change of thermal properties without omitting any imperceptible variation. The thermal conductivities along *c*-axis reveal an abrupt change around 255 K, indicating the phase transition near this temperature. More importantly, the thermal conductivities near the phase transition temperature show different values, i.e., the

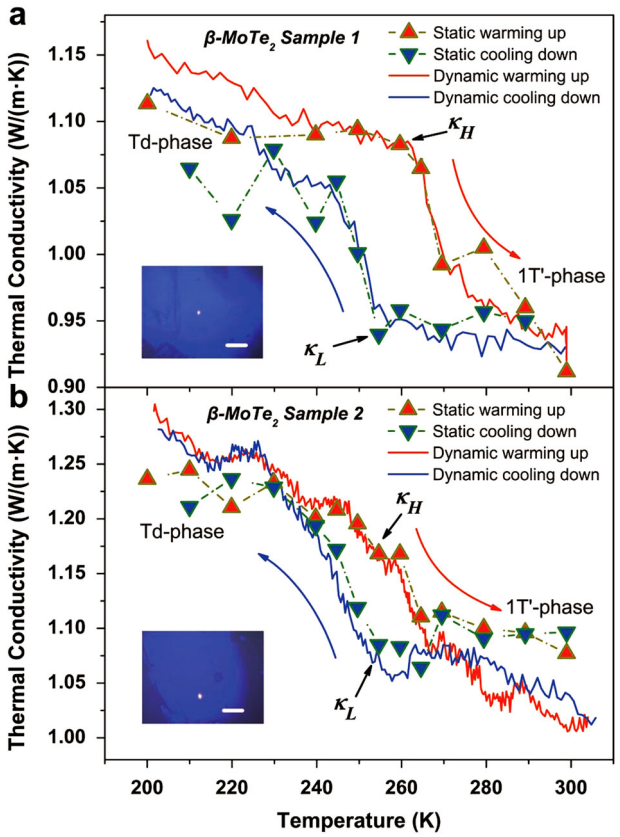

Fig. 3 **a** & **b** Hysteretic behaviors of *c*-axis thermal conductivity in the metastable phase $MoTe_2$ sample 1 & 2. The triangular scatters represent the experimental data measured by 'the static method', while the *solid lines* represent the results continuously measured by 'the dynamic method'. The *red* and *blue arrows* indicate the directions of warming up and cooling down routes, respectively. The inserted images show the locations of focused laser spots on the $MoTe_2$ samples during the TDTR measurements

higher one κ_H and the lower one κ_L in the warming up and cooling down routes, respectively. This is so-called thermal hysteresis of thermal conductivity, where values cannot recover in the opposite temperature evolution and a hysteresis loop is formed around 255 K.

To discover the origin of this thermal hysteresis, we carried out Raman spectroscopy measurements of the metastable state $MoTe_2$ in both the cooling down and warming up routes. From the Raman spectra in Fig. 4a, we found that a single mode near 130 cm^{-1} was transformed into two modes when sample was cooled down to ~230 K. It has been demonstrated that this new Raman mode D at ~127.8 cm^{-1} is a signature of the Td-phase, whose inversion symmetry of lattice structure is broken at low-temperatures.[19] When the sample was heated up to ~270 K, the peak of mode D disappeared (see Fig. 4b), revealing the reappearance of the 1T′-phase with an inversion symmetry. In Fig. 4c, we fit the peaks of Raman spectra near 130 cm^{-1} by Gaussian function to extract the revolution of Raman modes. When the sample is cooled down to 230 K, the single Raman peak broadens and it can be decomposed into multi-peaks, which depicts the co-existence of the 1T′-phase and Td phases.[17, 18] The co-existence of two phases can induce high-density phase boundaries in metastable state $MoTe_2$ as our theoretical analysis indicates. The fitted peak intensities of D-mode in both routes were summarized in Fig. 4d. The thermal hysteresis of D-mode peak intensity, i.e., the proportion of the Td-phase, was conspicuous in the temperature interval of 230–270 K. This temperature interval was qualitatively coincident with that of 240–260 K in the hysteretic properties of thermal and electrical transport shown in Fig. 3. The extended temperature range of the structural hysteresis was also observed in a high-resolution XRD study,[16] indicating the two phases can coexist in a wider temperature range than that shown in the transport property. A possible explanation might be that a higher activation energy is needed to overcome the potential barrier to enable the phase transition. We have experimentally verified that this hysteretic behavior is repeatable and consistent in multiple samples.

DISCUSSION

It has been demonstrated that PCMs with hysteretic behaviors in thermal conductivities could be applied in thermal memory prototypes.[4–6] To simplify, we conceptually describe how to realize the functions of a thermal memory using metastable $MoTe_2$ here. In the hysteresis loop, κ_H can be defined as the 'ON' state and κ_L is the 'OFF' state. A thermal memory device based on $MoTe_2$ can work at a stabilized temperature of 255 K. As we 'write' the thermal information by increasing (or decreasing) its temperature dynamically, the thermal conductivity of $MoTe_2$ will be κ_L (or κ_H) after it goes back to the equilibrium temperature 255 K. In this way, the nonvolatile storage of the 'OFF' (or 'ON') state is realized and we can 'read' the state by detecting its thermal conductivity or thermal transport properties. The difference $\Delta = \frac{\kappa_H - \kappa_L}{(\kappa_H + \kappa_L)/2}$ near the working temperature can be used to represent the remanence of the stored states.

The hysteresis in thermal conductivity has been observed and studied in VO_2,[7] NiTi,[39] $YBa_2Cu_3O_{7-x}$,[40] and $NbH_{0.87}$,[41] etc. The relative difference Δ is about 10% for $MoTe_2$ here, which is larger than those of $YBa_2Cu_3O_{7-x}$ & $NbH_{0.87}$ (~3%) and comparable to that of the representative PCM, VO_2 (6–20%).[7, 8] The thermal hysteresis in VO_2-induced by the metal insulator transition is dominated by electron transportation, while the contribution of electrons to the total thermal conductivity in *c*-axis is only ~6% in our $MoTe_2$ samples. Therefore, the hysteretic behavior of *c*-axis thermal conductivity in $MoTe_2$ is dominated by phonons. It means that $MoTe_2$ could be a more suitable material for the applications of thermal logic devices which are purely based on phonon transportations.[3, 9] Besides, it seems not difficult to control the chemical composition of the $MoTe_2$ samples, whose thermal hystereses show small variations from sample to sample in this paper. It will be a benefit to the consistency of device performance when $MoTe_2$ is applied in thermal memory devices. The layered TMDs can be mechanically exfoliated into one monolayer or a few layers, which provides the opportunities for its further applications in the integrated phononic devices.[13, 21] Moreover, it has been claimed that the electrostatic gating may induce the structural phase transitions of semiconductor-to-semimetal in the monolayer $MoTe_2$.[42, 43] A recent study discovered that the phase transition temperature can also be engineered through a W substitution in $MoTe_2$ samples.[44] In summary, the properties of thermal hysteresis in $MoTe_2$-based materials can be elaborately adjusted by electrostatic gating, chemical doping, or stoichiometric modulation for their practical applications.

In conclusion, we have measured the *c*-axis thermal conductivities of $MoTe_2$ samples synthesized by a CVT method. By means of the theoretical analysis based on BTE, we found the phonon scatterings in the 2H-$MoTe_2$ were dominated by the Umklapp process, while those in the metastable phase $MoTe_2$ were dominated by the boundary scatterings due to the high-density phase boundaries and stacking disorders. More importantly, the hysteresis in *c*-axis thermal conductivity of the metastable phase $MoTe_2$ was observed around 250 K, coincident with the thermal hysteresis effects in the Raman spectra and electrical resistivity characterized on the same samples. The largest difference of thermal conductivity in the hysteresis loop was comparable to

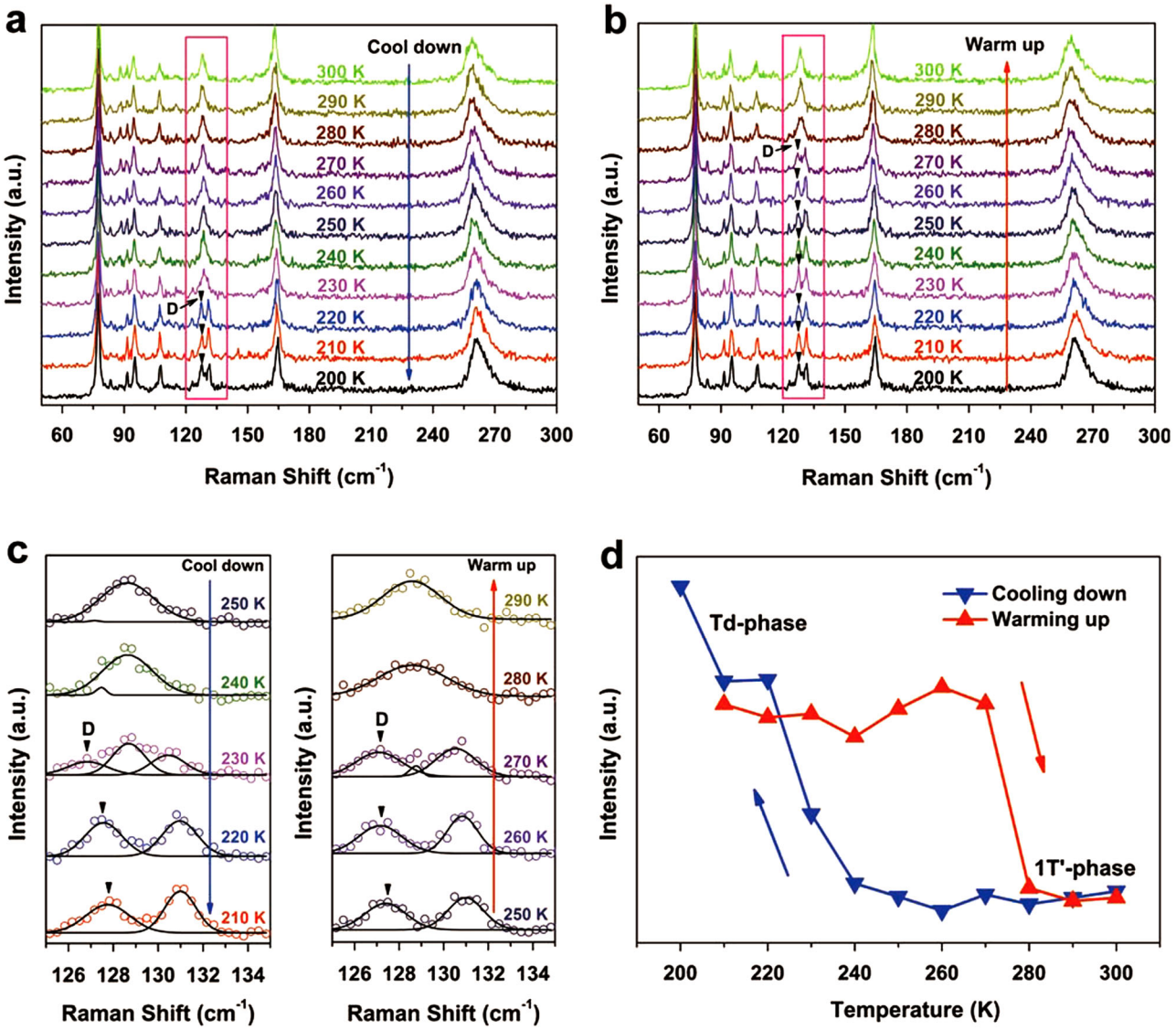

Fig. 4 **a** and **b** Raman spectra of metastable phase $MoTe_2$ at various temperatures in the cooling down **a** and warming up **b** routes. The D mode noted by *balck arrows* at ~127.8 cm^{-1} indicate the existence of Td-phase with a broken inversion symmetry. **c** Extended Raman spectra (*circular holes*) around 130 cm^{-1} fitted by the Gaussian function (*black solid lines*) near the temperature of phase transitions in the opposite routes. **d** Temperature dependence of the fitted intensities of Raman mode D in two opposite temperature routes which are indicated by *arrows*

that of the traditional PCMs, and the thermal transport along *c*-axis in $MoTe_2$ is dominated by phonons. Therefore, the material system studied here may be a promising candidate for all-phononic devices. This work shows an opportunity for the subsequent investigations in phononic devices, energy harvesting and thermal transport studies of low-dimensional TMDs.

METHODS

The 2H-$MoTe_2$ and β-$MoTe_2$ samples were prepared by the CVT method using Bromine (Br_2) as the transport agents similar to our previous report.[45] Firstly, $MoTe_2$ powders were synthesized by heating a stoichiometric mixture of Mo (99.99%) and Te (99.999%) powders at 750 °C in a sealed and evacuated quartz ampoule. Secondly, certain amount of the yielded $MoTe_2$ polycrystalline powders and ~5 mg cm^{-3} of Br_2 were mixed and loaded into another evacuated quartz ampoule, which was then placed into a two-zone furnace for the growth of samples (see figure S1 in the supplementary information). 2H-$MoTe_2$ crystals can be grown at a temperature profile of 700–800 °C and finished by cooling treatments in the ambient environment (100 °C/h). To get the metastable β-phase existing at high temperature, a higher temperature profile of 900–1000 °C was used during the synthesis process and then samples were quenched immediately in the ice water to room temperature to retain this high-temperature β-phase. The yielded 2H-$MoTe_2$ single crystal flakes possessed hexagonal shapes with dimensions about $5 \times 5 \times 0.05$ mm and β-$MoTe_2$ flakes possessed striped shapes with dimensions about $5 \times 0.5 \times 0.05$ mm (see Fig. 1b).

The 2H and β-$MoTe_2$ samples were characterized by the XRD measurements with 2θ scanned from 10° to 70° using the Cu-Kα radiation. The stoichiometric ratios of the as-grown crystals were determined by an EDS (Oxford) spectrometer equipped in a scanning electron microscope (ZEISS Ultra 55). Standard four-probe technique was used for the electrical resistivity measurements at low temperatures in a physical property measurement system (PPMS-9, Quantum Design). The Raman spectra were taken using a He-Ne laser as an optical source at 633 nm on a LabRam HR800 Microscope system (Horiba Jobin Yvon). The samples were cooled from 300 to 200 K by liquid nitrogen when taking Raman measurements in different temperature routes.

The thermal conductivities along *c*-axis of the layered $MoTe_2$ samples were measured by the TDTR method. TDTR is a convenient and non-contact method to measure the thermal conductivities of bulk materials,[46]

thin films,[47] and even liquid samples.[48] Before taking the TDTR measurements, each $MoTe_2$ sample was mechanically exfoliated to get a fresh surface and then coated with a ~80 nm thick aluminum (Al) film which serves as the optical transducer. The pulsed laser beam with a width of ~170 fs is separated into a pump beam and a probe beam with a relative time delay of 300–4000 ps. The pump beam heats up the surface of the Al film and then the probe beam profiles the time-domain evolution of temperature on the surface by detecting its optical reflectivity which is proportional to the temperature of the Al surface.[49] In practice, the reflected probe beam was captured by a Si photo detector and its output signal was analyzed by a radio frequency lock-in amplifier. We fitted the ratio of the in-phase (V_{in}) and out-of-phase (V_{out}) components of signal $-V_{in}/V_{out}$ by a diffusive thermal model to extract the thermal properties of the materials being tested.[50, 51] The 'double-frequency modulation' technique was utilized to improve the signal-to-noise ratio and a 'two-tint construction' was applied to eliminate the signal disturbance from the leaked pump beam.[52] The configuration for our TDTR system is depicted in Supplementary figure S2. We have measured a series of bulk and thin-film standard samples to verify the accuracy and reliability of our system. Particularly, we have also measured the thermal conductivity of 2H-WSe_2 single crystal to confirm the reliability of our TDTR measurements in such layered materials.[47] The details of our TDTR setup and the measured results for calibrations are summarized in the supplemental information. The lateral scale of the focused spot on the sample was only ~20 μm and the thermal penetration depth in $MoTe_2$ can be less than 100 nm due to the high modulation frequency (~9.8 MHz) of the pump beam. Therefore, TDTR measurement is suitable for our $MoTe_2$ thin flakes (thicknesses are ~50 μm) with small sizes (~5 × 5 mm), which are difficult to be measured by commercial instruments.

ACKNOWLEDGEMENTS

This work was jointly supported by the National Basic Research Program of China (No. 2017YFA0303700, No. 2013CB632904 and No. 2013CB632702), the National Nature Science Foundation of China (Grant No. 11134006, No. 11474158, No. 11404164, No. 11625418 and No. 51472114), and the Natural Science Foundation of Jiangsu Province (BK20140019). We also acknowledge the project funded by the Priority Academic Program Development of Jiangsu Higher Education (PAPD).

AUTHOR CONTRIBUTIONS

X.-J.Y. and M.-H.L. conceived the idea. X.-J.Y. and L.L. took the thermal conductivity measurements by TDTR method and analyzed the experimental data theoretically by BET. Y.-Y.L. performed the crystal growth with the guidance of S.-H.Y. and conducted the XRD measurements. X.-J.Y. and X.L. conducted the temperature-dependent Raman spectroscopy measurements. X.-J.Y. and Y.-Y.L. co-wrote the manuscript with revisions from other authors. H.L. and M.-H.L. guided the project. All authors contributed to the discussions and comments on the manuscript.

ADDITIONAL INFORMATION

Supplementary Information accompanies the paper on the *npj Quantum Materials* website (doi:10.1038/s41535-017-0031-x).

Competing interests: The authors declare that they have no competing financial interests.

Publisher's note: Springer Nature remains neutral with regard to jurisdictional claims in published maps and institutional affiliations.

REFERENCES

1. Wen, Z., Li, C., Wu, D., Li, A. & Ming, N. Ferroelectric-field-effect-enhanced electroresistance in metal/ferroelectric/semiconductor tunnel junctions. *Nat. Mater.* **12**, 617–621 (2013).
2. Fert, A. Nobel lecture: origin, development, and future of spintronics. *Rev. Mod. Phys.* **80**, 1517–1530 (2008).
3. Wang, L. & Li, B. Thermal memory: a storage of phononic information. *Phys. Rev. Lett.* **101**, 267203 (2008).
4. Kubytskyi, V., Biehs, S.-A. & Ben-Abdallah, P. Radiative bistability and thermal memory. *Phys. Rev. Lett.* **113**, 074301 (2014).
5. Pellegrino, L. et al. Multistate memory devices based on free-standing VO_2/TiO_2 microstructures driven by Joule self-heating. *Adv. Mater.* **24**, 2929–2934 (2012).
6. Ito, K., Nishikawa, K. & Iizuka, H. Multilevel radiative thermal memory realized by the hysteretic metal-insulator transition of vanadium dioxide. *Appl. Phys. Lett.* **108**, 053507 (2016).
7. Oh, D.-W., Ko, C., Ramanathan, S. & Cahill, D. G. Thermal conductivity and dynamic heat capacity across the metal-insulator transition in thin film VO_2. *Appl. Phys. Lett.* **96**, 151906 (2010).
8. Xie, R. et al. An electrically tuned solid-state thermal memory based on metal–insulator transition of single-crystalline VO_2 Nanobeams. *Adv. Funct. Mater.* **21**, 1602–1607 (2011).
9. Li, N. et al. Colloquium: phononics: manipulating heat flow with electronic analogs and beyond. *Rev. Mod. Phys.* **84**, 1045–1066 (2012).
10. Jeong, J. et al. Suppression of metal-insulator transition in VO_2 by electric field–induced oxygen vacancy formation. *Science* **339**, 1402–1405 (2013).
11. Zhu, J. et al. Temperature-gated thermal rectifier for active heat flow control. *Nano. Lett.* **14**, 4867–4872 (2014).
12 Ji, Y. et al. Role of microstructures on the M1-M2 phase transition in epitaxial VO_2 thin films. *Sci. Rep* **4**, 4854 (2014).
13. Keum, D. H. et al. Bandgap opening in few-layered monoclinic $MoTe_2$. *Nat. Phys* **11**, 482–486 (2015).
14. Hughes, H. & Friend, R. Electrical resistivity anomaly in β-$MoTe_2$ (metallic behaviour). *J. Phys. C: Solid State Phys* **11**, L103–L105 (1978).
15. Qi, Y. et al. Superconductivity in Weyl semimetal candidate $MoTe_2$. *Nat. Commun.* **7**, 11038 (2016).
16. Clarke, R., Marseglia, E. & Hughes, H. A low-temperature structural phase transition in β-$MoTe_2$. *Philos. Mag. B* **38**, 121–126 (1978).
17. Manolikas, C., Van Landuyt, J. & Amelinckx, S. Electron microscopy and electron diffraction study of the domain structures, the dislocation fine structure, and the phase transformations in β-$MoTe_2$. *Phys. Status Solidi A* **53**, 327–338 (1979).
18. Zhang, K. et al. Raman signatures of inversion symmetry breaking and structural phase transition in type-II Weyl semimetal $MoTe_2$. *Nat. Commun.* **7**, 13552 (2016).
19. Chen, S.-Y., Goldstein, T., Venkataraman, D., Ramasubramaniam, A. & Yan, J. Activation of new Raman modes by inversion symmetry breaking in type II Weyl semimetal candidate T′-$MoTe_2$. *Nano. Lett.* **16**, 5852–5860 (2016).
20. Wang, Q. H., Kalantar-Zadeh, K., Kis, A., Coleman, J. N. & Strano, M. S. Electronics and optoelectronics of two-dimensional transition metal dichalcogenides. *Nat. Nanotechnol* **7**, 699–712 (2012).
21. Qian, X., Liu, J., Fu, L. & Li, J. Quantum spin Hall effect in two-dimensional transition metal dichalcogenides. *Science* **346**, 1344–1347 (2014).
22. Soluyanov, A. A. et al. Type-II Weyl semimetals. *Nature* **527**, 495–498 (2015).
23. Sun, Y., Wu, S.-C., Ali, M. N., Felser, C. & Yan, B. Prediction of Weyl semimetal in orthorhombic $MoTe_2$. *Phys. Rev. B* **92**, 161107 (2015).
24. Wang, Z. et al. $MoTe_2$: a type-II Weyl topological metal. *Phys. Rev. Lett.* **117**, 056805 (2016).
25. Deng, K. et al. Experimental observation of topological Fermi arcs in type-II Weyl semimetal $MoTe_2$. *Nat. Phys* **12**, 1105–1110 (2016).
26. Ma, Y. et al. Quantum spin Hall effect and topological phase transition in two-dimensional square transition-metal dichalcogenides. *Phys. Rev. B* **92**, 085427 (2015).
27. Choe, D.-H., Sung, H.-J. & Chang, K. Understanding topological phase transition in monolayer transition metal dichalcogenides. *Phys. Rev. B* **93**, 125109 (2016).
28. Puotinen, D. & Newnham, R. The crystal structure of $MoTe_2$. *Acta Crystallogr.* **14**, 691–692 (1961).
29. Brown, B. E. The crystal structures of WTe_2 and high-temperature $MoTe_2$. *Acta Crystallogr.* **20**, 268–274 (1966).
30. El-Mahalawy, S. & Evans, B. Temperature dependence of the electrical conductivity and hall coefficient in 2H-MoS_2, $MoSe_2$, WSe_2, and $MoTe_2$. *Phys. Status Solidi B* **79**, 713–722 (1977).
31. Minnich, A. Phonon heat conduction in layered anisotropic crystals. *Phys. Rev. B* **91**, 085206 (2015).
32. Hsieh, W.-P., Chen, B., Li, J., Keblinski, P. & Cahill, D. G. Pressure tuning of the thermal conductivity of the layered muscovite crystal. *Phys. Rev. B* **80**, 180302 (2009).
33. Chen, Z., Wei, Z., Chen, Y. & Dames, C. Anisotropic Debye model for the thermal boundary conductance. *Phys. Rev. B* **87**, 125426 (2013).
34. Slack, G. A. & Galginaitis, S. Thermal conductivity and phonon scattering by magnetic impurities in CdTe. *Phys. Rev.* **133**, A253–A268 (1964).
35. Chen, F. C. et al. Superconductivity enhancement in the S-doped Weyl semimetal candidate $MoTe_2$. *Appl. Phys. Lett.* **108**, 162601 (2016).
36. Erhart, P., Hyldgaard, P. & Lindroth, D. O. Microscopic origin of thermal conductivity reduction in disordered van der Waals solids. *Chem. Mater.* **27**, 5511–5518 (2015).

37. Ding, Y. & Xiao, B. Thermal expansion tensors, Grüneisen parameters and phonon velocities of bulk MT_2 (M = W and Mo; T = S and Se) from first principles calculations. *RSC Adv.* **5**, 18391–18400 (2015).
38. Zhu, G. et al. Tuning thermal conductivity in molybdenum disulfide by electrochemical intercalation. *Nat. Commun.* **7**, 13211 (2016).
39. Ingale, B. D., Wei, W. C., Chang, P. C., Kuo, Y. K. & Wu, S. K. Anomalous transport and thermal properties of NiTi and with Cu and Fe-doped shape memory alloys near the martensitic transition. *J. Appl. Phys.* **110**, 113721 (2011).
40. Jeżowski, A. Evidence for hysteresis behaviour and anomaly of thermal conductivity in Y-Ba-Cu-O superconductor. *Solid State Commun* **71**, 419–424 (1989).
41. Misiorek, H., Jeżowski, A., Mucha, J. & Sorokina, N. Hysteresis of thermal conductivity and electrical resistivity of niobium hydrides. *Solid State Commun* **85**, 907–910 (1993).
42. Li, Y., Duerloo, K.-A. N., Wauson, K. & Reed, E. J. Structural semiconductor-to-semimetal phase transition in two-dimensional materials induced by electrostatic gating. *Nat. Commun.* **7**, 10671 (2016).
43. Zhang, C. et al. Charge Mediated Reversible Metal-Insulator Transition in Monolayer $MoTe_2$ and $W_xMo_{1-x}Te_2$ Alloy. *ACS Nano* **10**, 7370–7375 (2016).
44. Rhodes, D. et al. Engineering the structural and electronic phases of $MoTe_2$ through W substitution. *Nano Lett.* **17**, 1616–1622 (2017).
45. Lv, Y.-Y. et al. Dramatically decreased magnetoresistance in non-stoichiometric WTe_2 crystals. *Sci. Rep* **6**, 26903 (2016).
46. Schmidt, A. J., Chen, X. & Chen, G. Pulse accumulation, radial heat conduction, and anisotropic thermal conductivity in pump-probe transient thermoreflectance. *Rev. Sci. Instrum.* **79**, 114902 (2008).
47. Chiritescu, C. et al. Ultralow thermal conductivity in disordered, layered WSe_2 crystals. *Science* **315**, 351–353 (2007).
48. Schmidt, A., Chiesa, M., Chen, X. & Chen, G. An optical pump-probe technique for measuring the thermal conductivity of liquids. *Rev. Sci. Instrum.* **79**, 064902 (2008).
49. Wilson, R., Apgar, B. A., Martin, L. W. & Cahill, D. G. Thermoreflectance of metal transducers for optical pump-probe studies of thermal properties. *Opt. Express.* **20**, 28829–28838 (2012).
50. Cahill, D. G. Analysis of heat flow in layered structures for time-domain thermoreflectance. *Rev. Sci. Instrum.* **75**, 5119–5122 (2004).
51. Feser, J. P. & Cahill, D. G. Probing anisotropic heat transport using time-domain thermoreflectance with offset laser spots. *Rev. Sci. Instrum.* **83**, 104901 (2012).
52. Kang, K., Koh, Y. K., Chiritescu, C., Zheng, X. & Cahill, D. G. Two-tint pump-probe measurements using a femtosecond laser oscillator and sharp-edged optical filters. *Rev. Sci. Instrum.* **79**, 114901 (2008).